PAPER

Contrasting the characteristics of atmospheric pressure plasma jets operated with single and double dielectric material: physicochemical characteristics and application to bacterial killing

To cite this article: Bhagirath Ghimire et al 2023 J. Phys. D: Appl. Phys. 56 085205

View the article online for updates and enhancements.

You may also like

- Development of a small-scale helical surface dielectric barrier discharge for characterizing plasma—surface interfaces Nazli Turan, Patrick M Barboun, Pritam K Nayak et al.
- Dry reforming of methane via plasmacatalysis: influence of the catalyst nature supported on alumina in a packed-bed DBD configuration L Brune, A Ozkan, E Genty et al.
- Decomposition of dioxin-like components in a DBD reactor combined with Hg/Ar electrodeless ultraviolet Weixuan ZHAO, , Liping LIAN et al.

Contrasting the characteristics of atmospheric pressure plasma jets operated with single and double dielectric material: physicochemical characteristics and application to bacterial killing

Bhagirath Ghimire^{1,2,*}, Elanie F Briggs³, Tatyana A Sysoeva³, John A Mayo³ and Kunning G Xu^{2,*}

E-mail: bhagirath.ghimire@uah.edu and gabe.xu@uah.edu

Received 15 November 2022, revised 18 January 2023 Accepted for publication 25 January 2023 Published 10 February 2023



Abstract

This study reports an experimental comparison of two types of atmospheric pressure plasma jets in terms of their fundamental plasma characteristics and efficacy in bacterial sterilization. The plasma jets are fabricated by inserting a high voltage electrode inside a one-end closed (double DBD plasma jet) or both ends open (single DBD plasma jet) quartz tubes which are further enclosed inside a second quartz tube containing a ground electrode. Both plasma jets are operated in contact with water surface by using a unipolar pulsed DC power supply with helium as the working gas. Results from electrical and time-resolved imaging show that the single DBD configuration induces 3-4 times higher accumulation of charges onto the water surface with significantly faster propagation of plasma bullets. These results are accompanied by the higher discharge intensity as well as stronger emissions from short-lived reactive species which were analyzed through optical emission spectroscopy at the plasma-water interface. The rotational temperature for the single DBD configuration was observed to be higher making it unsafe for direct treatments of sensitive biological targets. These characteristics of the single DBD configuration result in the production of more than two times higher concentration of H₂O₂ in plasma activated water. Shielding of the HV electrode reduces the plasma potential which in turn reduces the electric field & electron energy at the plasma-water interface. The reduced electric field for the double DBD configuration was lower by \approx 463 Td than the single DBD configuration. The bactericidal efficacy of the two configurations of the plasma jets were tested against Escherichia coli, a well studied Gram-negative bacterium that

1

¹ Center for Space Plasma and Aeronomic Research, University of Alabama in Huntsville, Huntsville, AL 35899, United States of America

² Department of Mechanical and Aerospace Engineering, University of Alabama in Huntsville, Huntsville, AL 35899, United States of America

³ Department of Biological Sciences, University of Alabama in Huntsville, Huntsville, AL 35899, United States of America

^{*} Authors to whom any correspondence should be addressed.

can be commensal and pathogenic in human body. Our results demonstrate that although single DBD plasma jet result in stronger antibacterial effects, the double DBD configuration could be safer.

Keywords: atmospheric pressure plasma jets, plasma medicine, optical emission spectroscopy, hydrogen peroxide, bacterial sterilization, plasma diagnostics, Antimicrobial effects

(Some figures may appear in colour only in the online journal)

1. Introduction

In the last two decades, there has been increasing interest over the use of atmospheric pressure plasma jets (APPJs) for biological and medical applications including wound healing, sterilization of surfaces, blood coagulation, root canal treatment and cancer treatment [1–6]. APPJs are useful in these applications as they generate reactive oxygen species (ROS) and reactive nitrogen species (RNS) through the interaction of electrons, ions, and excited species with ambient species [7–9], while remaining at or near room temperature. The synergistic action of ROS and RNS (together called reactive oxygen and nitrogen species (RONS)) is known to be highly effective in decontaminating a range of pathogenic bacteria important for medical applications [3, 10].

The APPJs used for the production of RONS usually consist of a high voltage electrode and a ground electrode that are separated by a spacing up to few centimetres within a dielectric tube [11–13]. Upon application of a sufficient electric field, the gas between the electrodes is ionized, creating energetic electrons and ions that lead to the formation of different RONS in the presence of parent species such as water, oxygen, and nitrogen via electrochemistry. The RONS are then carried to the downstream application region. APPJs are easy to construct and as a result many different jet configurations have been reported. In one commonly used configuration, the internal high voltage (HV) electrode is enclosed inside a dielectric material which is further surrounded by a second dielectric material [14, 15]. In another commonly used configuration, a single dielectric material separates the HV and the ground electrode [11, 16]. Both configurations of the plasma jets have been studied for different applications including biomedicine and water purification [17-21]. Despite the scale of their applications, there is considerable ambiguity as to their relative characteristics and merits for the aforementioned applications, thus making direct comparisons between studies difficult. This ambiguity also highlights an important knowledge gap in APPJ physics and chemistry. In this article, the effect of dielectric shielding of the HV electrode on the characteristics of an atmospheric pressure helium plasma jet is investigated. Two identical plasma jets, the first one with one dielectric material between the HV and the ground electrode (termed as single dielectric barrier discharge (DBD) plasma jet) and the second one with two dielectric materials between the HV and the ground electrode (termed as double DBD plasma jet) are constructed to investigate their physicochemical properties in contact with water surface at identical operating conditions. The antibacterial efficacy of the two APPJs in a real-world application is then demonstrated by applying the plasma jets to kill *E. coli* (*E. coli*), pathogenic strains of which can be found in the human body.

2. Experimental methodology

2.1. Plasma jet setup

The schematics of the double and single DBD configurations of the plasma jets along with the overall setup of the experimental setup are shown in figure 1. The plasma jets were constructed by inserting a tungsten electrode (length = 76 mm, outer diameter, OD = 1 mm) inside an inner quartz tube (inner diameter, ID = 2 mm, OD = 3.10 mm). This acted as the HV electrode. The bottom end of this inner quartz tube in the first plasma jet is closed (figure 1(a), double DBD configuration), while it is open in the second plasma jet (figure 1(b), single DBD configuration). The distance between the end of the tungsten electrode and the end of the inner quartz tube is 2 mm. The setup is then inserted inside a 1/4'' nylon Tee compression fitting (Swagelok). A second or outer quartz tube (ID = 4 mm, OD = 6 mm, length = 45 mm) enclosed the inner tube and the tungsten electrode within the Tee fitting. Copper tape is wrapped around the outer tube and used as the ground electrode (length $= 6 \, \text{mm}$) and placed 2 mm below the tip of the HV electrode. The length of the outer quartz tube below the ground is 15 mm. Plasma is generated with an electrical setup (figure 1(c)) consisting of a SRS DG-645 digital delay generator (DDG), a unipolar Matsusada +10 kV DC power supply, and a DEI-PVX-4110 pulse generator with a rise and fall time of 60 ns. The working gas was helium (He) with a purity of >99.999 % and was metered by a mass flow controller (Model: GE50A013503SBV020, MKS Instruments Inc.)) into the Tee. Both plasma jets were operated at a fixed applied voltage of 7 kV, frequency of 6 kHz, and at a pulse width of 1 μ s in freestream mode and in contact with distilled water (conductivity = 1.8 μ S cm⁻¹) placed inside a petri-dish. The volume of water inside the petri-dish was 25 ml and the distance between the nozzle of the quartz tube and water surface was 12 mm. Helium was flowed at a constant flow rate of 2 standard liters per minute (SLPM) in both plasma jets.

2.2. Measurement of Electrical Signals

Electrical signals during the discharge were acquired by connecting a Tektronix voltage probe (Model no. P6015) to the HV tungsten electrode and a Pearson current probe (Model no. 2100) to the ground electrode. The signals from the voltage

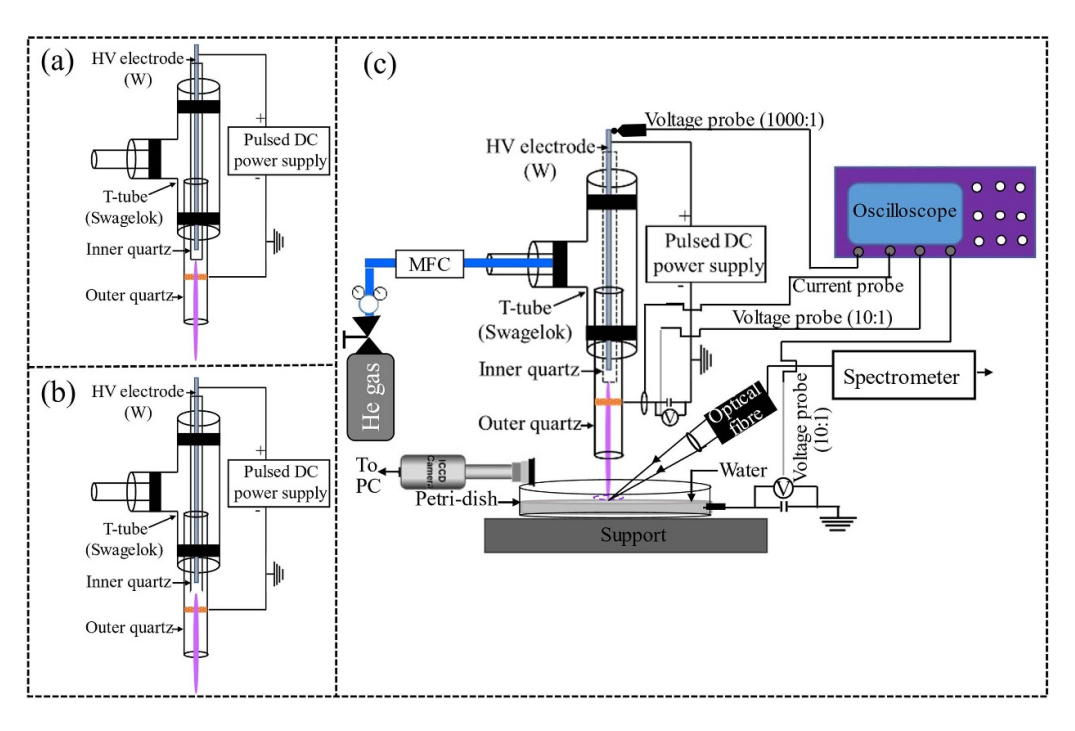


Figure 1. Schematics of the (a) double; (b) single DBD configuration of the plasma jets; and (c) overall setup of the experiment.

and current probes were recorded in an oscilloscope (Tektronix MDO3024). During the discharge process, significant charges could be accumulated on the internal surface of the quartz tube and also could be carried to the water surface during the propagation of the plasma bullet. These charges were measured simultaneously from the ground (copper electrode wrapped outside of the quartz tube) and from inside the water. For this purpose, two capacitors—each of size $3.34\,\mathrm{pF}$ were connected in series with the ground electrode and the target liquid respectively. A copper wire (diameter $\approx 2\,\mathrm{mm}$) remained in contact with the water layer through a hole drilled and sealed within the petri-dish. The signals from each capacitors were carried to the four-channel oscilloscope with two identical 10:1 voltage probes.

2.3. Time-resolved imaging

The time-resolved images of the double and single DBD plasma jets were obtained in freestream mode and in contact with water surface. The signals were recorded by using an Andor iStar 334T intensified charged coupled device (ICCD) camera. The camera was synchronized with the trigger signal from the DDG that also drives the pulse generator. The images were recorded at various delay times since the start of plasma bullet formation with the following settings in the ICCD camera: TTL width = 30 ns, accumulation = 1 and exposure time = $10 \mu s$ and MCP gain = 4000.

2.4. Optical emission spectroscopy

Optical emission spectra (OES) of the double and single DBD plasma jets were recorded using a 0.5 m Princeton

Instruments SP2500 spectrometer coupled to a PI-MAX 4 1024×256 pixel ICCD camera. The spectrometer was calibrated in wavelength and intensity using the manufacturer provided calibration lamps (Intellical, Princeton Instruments). The spectra were recorded by focusing a lens (focal length $10~\rm cm$, inclination 45°) to the plasma-water interface. The discharge region above the interface was blocked with a black tape to only acquire the signals from the interface region. In order to obtain the time resolved optical emission intensities, the camera was synchronized with the DDG that also drives the pulse generator.

2.5. Measurement of RONS formed inside water

To understand the application effect of the double and single DBD plasma jets, we investigated the production of hydrogen peroxide (H₂O₂), a relatively stable molecule formed through the recombination reactions between highly reactive hydroxyl (*OH) radicals in plasma activated water (PAW). Preparation of PAW was done by treating a volume of 350 μ l of distilled water (DIW) in a well of a 96-well plate for (a) different plasma exposure time (1, 3, 5 min) at a fixed He flow rate of 2 SLPM; and (b) He flow rates of 2 & 4 SLPM at a fixed plasma exposure time of 3 min. The distance between the end of the quartz tube and the surface of distilled water was set to 12 mm. Firstly, a calibration curve with known concentrations of H₂O₂ was constructed by using a colorimetric assay based on o-phenylenediamine (OPD, CAS number: 95-54-5, Sigma Aldrich Corporation) and horseradish peroxidase (HRP, CAS number: 9003-99-0, Sigma Aldrich Corporation). Reagents were prepared by dissolving OPD and 20 μ l of 2 mg ml⁻¹ HRP in 10 ml of DIW. HRP catalyses the oxidation of OPD in the presence of $\rm H_2O_2$ to form 2 to 3 diaminophenazine with an absorbance maximum of 450 nm [20, 22]. The absorbance maxima was measured using a plate reader (SpectraMax iD5, Molecular Devices). The line of best fit obtained with the calibration curve was then used to estimate the $\rm H_2O_2$ concentration in PAW. We also obtained a quantitative measurement of nitrites ($\rm NO_2^-$) using Griess-reagent (CAS number: 1465-25-4, Sigma Aldrich Corporation) to get insights on the concentration of RNS that could be formed by double and single DBD configurations of the plasma jets inside water.

2.6. Bacterial culture

Non-pathogenic E. coli (MG1655-pRK100) was obtained from the Sysoeva lab (Department of Biological Sciences, University of Alabama in Huntsville) strain collection. This strain was streaked out from the frozen glycerol stock onto lysogeny broth (LB) agar plate and grown at 37 °C overnight. A colony from this plate was inoculated into 4 ml of nutrient rich LB media and this E. coli culture was grown overnight with aeration (250 rpm) at 37 °C. The optical density at 600 nm (OD₆₀₀) was measured and used to adjust cell density to load onto fresh LB agar plates for consecutive plasma treatment. An OD_{600} of 1 corresponded to 10^8 colony forming units (CFUs) per ml. Cell suspension were prepared and spread over the LB agar using sterile glass beads to achieve the final surface cell density of 10², 10⁴ or 10⁶ CFU cm⁻². During plasma treatment, each plate was placed at the fixed height pedestal secured and balanced under the double/single DBD APPJ assembly such that the distance between the plasma jet nozzle and agar plate surface was 12 mm. Each plates were treated at (a) plasma exposures time of 1, 3 and 5 min at a fixed He flow rate of 2 SLPM; and (b) He flow rates of 2 & 4 SLPM at a fixed plasma exposure time of 3 min. The plates were then incubated agar-up at 37 °C overnight and then imaged. The clearance zones—zones of inhibition (ZoI) that were devoid of bacterial growth were measured in GIMP software as diameter of the maximal circle without any growth. Triplicate measurements of each treatment were collected and means and standard deviations calculated.

3. Results & discussion

The results in this paper are presented to illustrate how the shielding of a high voltage electrode influences the plasma characteristics (electrical/optical/time-resolved) and how this influences the production of RONS in plasma activated water. The importance of double and single DBD configurations of the plasma jets for practical application is then demonstrated by comparing their ability to inactivate *E. coli*.

3.1. Plasma plume lengths

Figures 2(a) and (b) shows photographs of the double and single DBD plasma jets launched into ambient air. The lengths

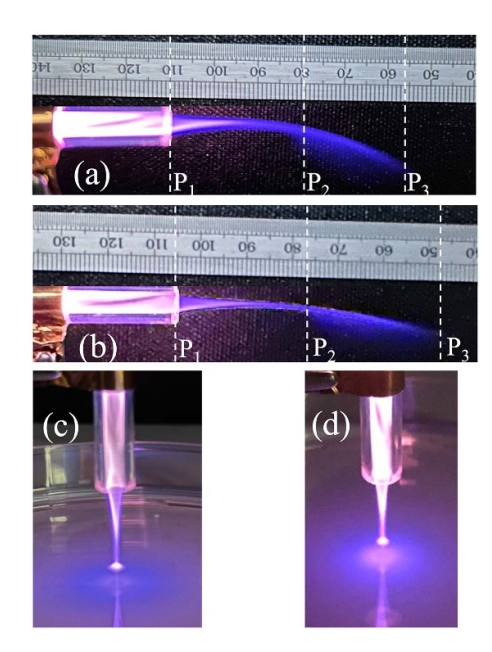


Figure 2. Photographs of the (a), (c) double; and (b), (d) single DBD plasma jets in freestream (a), (b) mode and in contact with water surface (c), (d) (Operating conditions: applied voltage—7 kV, frequency—6 kHz, pulse width—1 μ s, He flow rate—2 SLPM). Points P_1 , P_2 and P_3 in (a), (b) respectively represent quartz tube's nozzle, the point at which plasma bullet starts bending and maximum distance travelled by the plasma jet.

of the plasma plumes for double and single DBD plasma jets are measured to be 58 mm and 54 mm respectively. In both configurations, the plasma plume starts to bend and the diameter increases at \approx 30 mm below the nozzle of the quartz tube (point P_2 in figures 2(a) and (b)). Also, the brightness of the double DBD plasma jet was observed to be higher while in contact with water (figures 2(c) and (d)). Additional characteristics of the plasma jets will be investigated using time-resolved imaging in the next section.

3.2. Electrical characteristics

Figures 3(a) and (b) shows the current (I) and voltage (V)waveforms of a single pulse discharge for the double and single DBD configurations of the plasma jet in contact with water surface. The voltage signals were measured at the HV tungsten electrode while the current signals were measured at the ground electrode. The peak value of current for the single DBD plasma jet during the rise time of the applied voltage was \approx 474 mA (figure 3(b)). This is two times higher than the peak value of current measured for the double DBD plasma jet $(\approx 236 \text{ mA})$ (figure 3(a)). The positive discharge current peak in figures 3(a) and (b) occur through the accumulation of wall charges on the inner surface of the quartz tube(s) during the rising part of the applied voltage. These charges are reversed in polarity during the falling part of the voltage, which gives rise to the negative discharge current peak. Also, during the operation of the plasma jets in contact with the water surface, a part

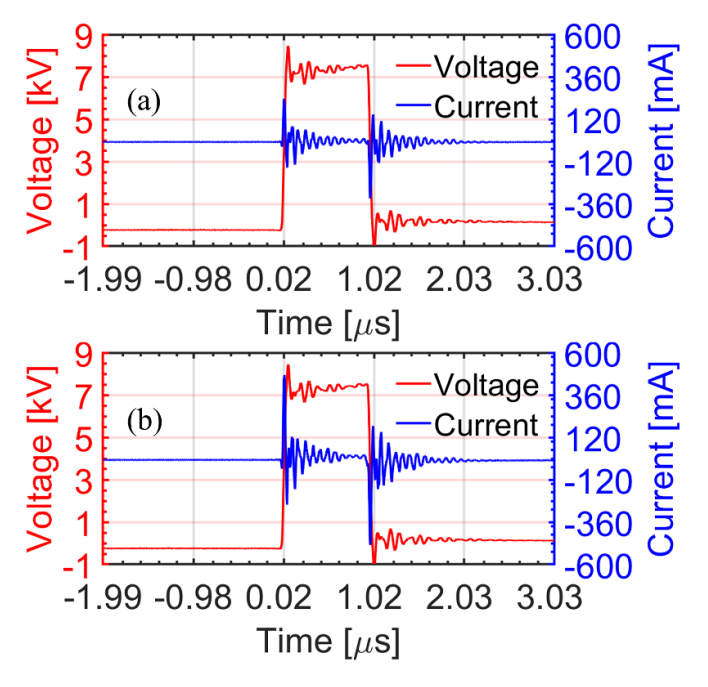


Figure 3. I–V waveforms measured for the double and single DBD plasma jets in contact with water surface. The voltage signals were measured at the HV electrode while the current signals were measured at the ground electrode. Operating conditions: applied voltage—7 kV, frequency—6 kHz, pulse width—1 μ s, He flow rate—2 SLPM.

of the current flows through the ground electrode while some part of the current flows towards the surface of water. Due to this phenomena, there could be some charges accumulated inside the water surface. In order to validate this hypothesis, the charges (Q) deposited on the inner walls of the quartz tube and those inside the water were measured simultaneously (also see figure 1). These results are presented in figure 4. At the position of the ground electrode (figure 4(a)), the maximum accumulated charges for the double and single DBD configurations of the plasma jets were measured to be 0.40 ± 0.01 nC and 0.75 \pm 0.005 nC respectively. The significant charge accumulation in the single DBD plasma jet starts at an applied voltage of \approx 2.75 kV followed by the initiation of the discharge, while for the double DBD configuration this starts at \approx 4 kV. The higher voltage for the double DBD configuration is due to the presence of additional dielectric material covering the HV electrode. When observed through the water surface (figure 4(b)), the maximum accumulated charges for the double and single DBD configurations were measured to be 2.20 \pm 0.13 nC and $7.51 \pm 1.08\,\mathrm{nC}$ respectively. These results suggest that significant charges could be transported with the plasma plume and deposited onto the surface of water during operation of the plasma jet in contact mode with the water surface. The maximum accumulated charges for the single DBD configuration are higher by approximately 2 times and 3-4 times on the inner walls of the quartz tubes and inside the water surface, respectively. One potential reason for the higher accumulation of charges in the change in the potential of the plasma

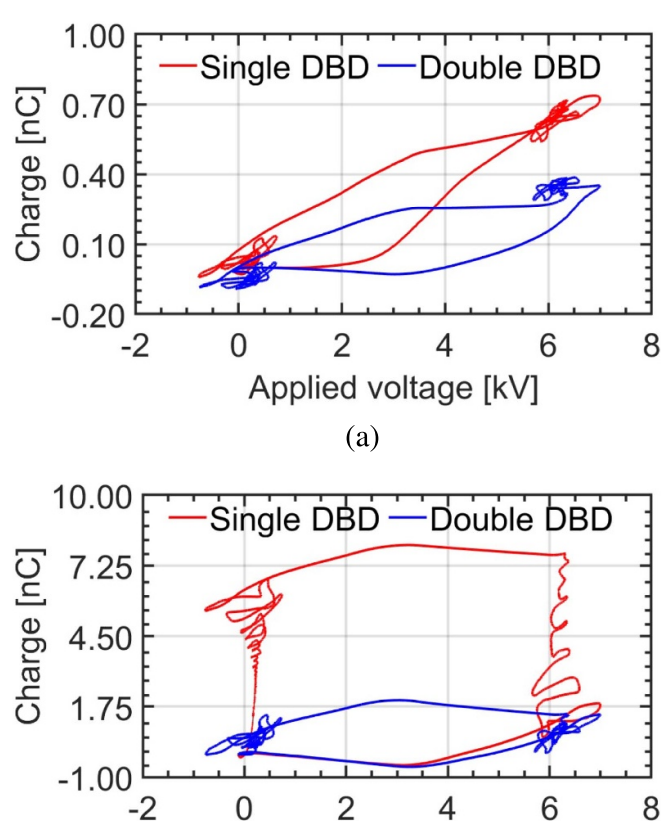


Figure 4. Comparison of the Q-V plots measured for the double and single DBD plasma jets through (a) the ground electrode and (b) the water placed inside the petri-dish. The measurement of charges at the two positions was done simultaneously.

Applied voltage [kV]

(b)

jet. In the case of single DBD configuration, the plasma potential is expectedly similar with the potential of the HV electrode while the internal dielectric material in the double DBD configuration reduces the potential of the plasma jet. As a result, less charge is expected to accumulate with the double DBD configuration [23]. These accumulated charges could induce higher electric field resulting in the longer length of the plasma plume (figure 2) and could also increase the chemical reactivity of the plasma [24].

The Q-V plots as shown in figure 4 were utilized to calculate the dissipated power (*P*) as:

$$P = f \times \text{Area of Q-V plot} = f \times \int Q dV$$
 (1)

where, f represents the frequency. The calculation of the area inside the closed Q-V plot was done through the integration of Q w.r.t. V using the trapezoidal rule in MATLAB. At the position of the ground electrode, the dissipated power calculated using equation (1) were found to be close to each other (9.01 \pm 3.71 mW and 10.01 \pm 3.85 mW for the double and single DBD configurations respectively). Similarly, the

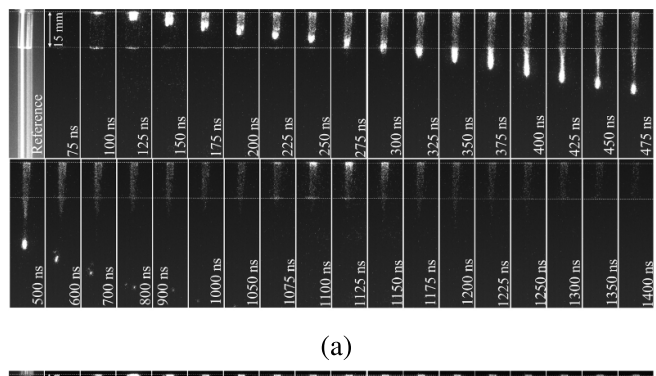
dissipated power calculated using the Q-V plots from the water was found to be 109.54 ± 39.26 mW and 427.99 ± 150.23 mW for the double and single DBD plasma jets respectively.

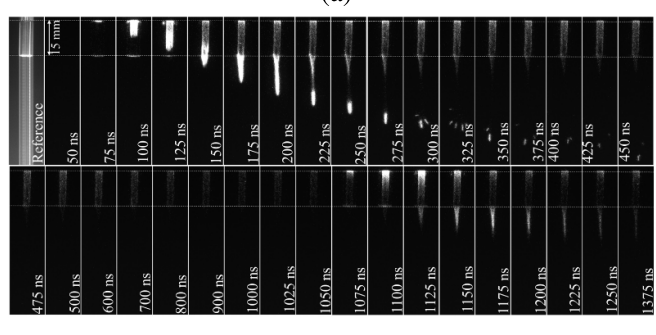
3.3. Time-resolved imaging

Time-resolved imaging in APPJs is an important technique to understand the dynamics of discharge emissions that take place at nanosecond timescales. As it is known that the contact of the plasma with the target material significantly influences the plasma propagation [25], we have investigated the propagation of plasma bullets for the double and single DBD configurations of the plasma jet in freestream mode as well as in contact with the surface of water. The images have been captured using an Andor iStar 334T ICCD camera synchronized with the trigger signal from the DDG that also drives the pulse generator.

Figure 5(a) shows the time resolved images obtained for the double DBD plasma jet in freestream mode. The first emission below the ground electrode is detected at a delay time of ≈ 100 ns. This bullet then reaches the nozzle of the quartz tube at \approx 300 ns and at an average velocity of 7.5 \times 10⁴ m s⁻¹. After that, it continues propagating with a bright emission in ambient air forming the classic plasma bullet. At \approx 600 ns, the plasma bullet has travelled \approx 27 mm from the nozzle of the quartz tube and it starts splitting into fragments. These fragments are seen to travel individually in the downstream region after 600 ns. The individual fragments dissipate during collision with ambient air molecules as they stay or travel more in ambient air. No emission is detected as the delay time reaches 1050 ns. At 1075 ns, a secondary glow appears below the ground electrode. Its intensity becomes weaker after 1125 ns, and no glow is recorded afterwards. The appearance of the secondary emission at 1075 ns is due to the release of accumulated charges on the inner walls of the quartz tube. This could be verified as the pulse width of the discharge (figure 3) is 1 μ s and the secondary emission also appears at $\approx 1 \,\mu s$ after the appearance of the first emission below the ground electrode.

The behavior of the plasma bullet propagation for the single DBD plasma jet in freestream mode is shown in figure 5(b). As compared to the double DBD plasma jet configuration, the plasma bullet is seen to travel faster and dissipate much earlier, before the falling edge of the applied voltage. The first emission near the ground electrode in figure 5(b) is recorded at \approx 75 ns. By 150 ns, the bullet is seen to have already crossed the exit of the outer quartz tube. The speed of the bullet exiting the quartz tube considering the moment it first appeared near the ground electrode is $\geq 2.5 \times 10^5$ m s⁻¹. The bullet continues propagating in ambient air with a bright emission until 275 ns. At 300 ns, the plasma bullet has travelled \approx 29 mm from the nozzle of the quartz tube and it is seen to split into at least two fragments. More splitted fragments from the bullet are observed at 325 ns. The emission from the fragments then weakens and no emission from the bullets is recorded afterwards. At 1075 ns (i.e. exactly 1 μ s after the appearance of the primary discharge emission), a secondary





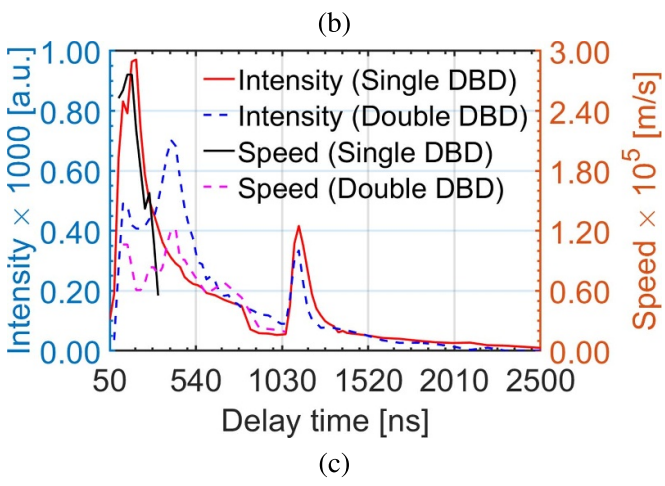


Figure 5. Temporal evolution of plasma bullets in a (a) double DBD and (b) single DBD plasma jet in freestream mode. The first dotted line on each rows represent the bottom of the ground electrode and the second dotted line represents the nozzle of the quartz tube. Each image is obtained with single shot at a TTL gate width of 30 ns and exposure time of 1 μ s (Operating conditions: applied voltage—7 kV, frequency—6 kHz, pulse width—1 μ s, He flow rate—2 SLPM). A plot of pixel intensities and propagation speeds computed from corresponding images in (a), (b) are shown in (c).

emission is observed below the ground electrode. This emission is observed to be stronger than the double DBD plasma jet and lasts until 1250 ns.

A plot of pixel intensities and plasma bullet propagation speeds derived from figures 5(a) and (b) for the double and single DBD plasma jets against different delay times are summarized in figure 5(c). The maximum intensity for single DBD configuration occurs at a delay time of 200 ns while for the double DBD configuration, it occurs at 400 ns. These time points in figures 5(a) and (b) correspond to the time at which the plasma bullet formed during the rising part of

the applied voltage has just exited the nozzle of the quartz tube. The emission intensity then decreases and another maxima, with lower intensity than the previous one is observed at 1125 ns. This maxima corresponds secondary discharge due to the accumulated charges inside the quartz tube. The maximum pixel intensity in both primary and secondary discharges are higher for the single DBD plasma jet. Also, it can be seen in figure 5(c) that the propagation speed for the single DBD plasma jet remains higher until the plasma bullet travels along the quartz tube and it continues to decrease afterwards. A similar phenomena is observed for the double DBD configuration. We also observe that the speed of plasma bullets for the single DBD plasma jet is much higher than the double DBD plasma jet. These values were measured to be: $7.5 \times 10^4 \text{ m s}^{-1}$ & $\geqslant\!\!2.5\times10^5~\text{m}\,\text{s}^{-1}$ (at the quartz tube's nozzle) and 8.31 \times 10^4 m s⁻¹ and $\ge 1.94 \times 10^5$ m s⁻¹ (in ambient air before splitting into fragments) for the double and single DBD plasma jets respectively. The higher speeds could be the result of higher electric field & higher plasma potential caused through higher accumulation of wall charges inside the quartz tube. Previous studies [26, 27] also suggest the strong dependence of plasma potential in the propagation of the plasma bullets. In our case, the shielding of the HV electrode could reduce the plasma potential and result in the significant reduction of the speed of plasma propagation.

In figures 5(a) and (b), the plasma bullet starts splitting into fragments after it has travelled a distance of \approx 27–29 mm below the nozzle of the quartz tube in both double and single DBD configurations of the plasma jets. This also corresponds to the point (point P_2 in figure 2) at which plasma plume starts bending. As the flow rate of helium in both plasma jets is the same and the plasma jets were designed in identical configuration, we speculate this to have happened due to the quenching by air molecules (mostly oxygen) diffusing into the ionization channel [28, 29].

The dynamics of plasma bullet propagation for the double and single DBD plasma jets in contact with water surface are represented in figures 6(a) and (b). The intensities of discharge emission at different delay times and measurable velocities are summarized in figure 6(c). The acquisition settings in the ICCD camera were the same as those in figure 5. For the double DBD configuration (figure 6(a)), the first emission below the ground electrode is detected at a delay time of 100 ns. The bullet travels along the quartz tube at a velocity of \approx 7.5–9.0 \times 10⁴ m s⁻¹ until it reaches the nozzle of the quartz tube (300 ns). After 325 ns, its speed suddenly increases to $1.07 \times 10^5 \text{ m s}^{-1}$ as it exits the nozzle of the quartz tube. The sudden increase in the speed is due to the presence of water in the downstream region which acts as second ground. The speed of the plasma bullet further increases to $1.67 \times 10^5 \text{ m s}^{-1}$ at 375 and the plasma bullet splashes in water. At this point, a bright emission is observed in the region between the nozzle of the quartz tube and water surface. The emission intensity in the discharge region then weakens. At \approx 1100 ns, the accumulated charges inside the quartz tube result in the formation of secondary discharge. This emission is only observed below the ground

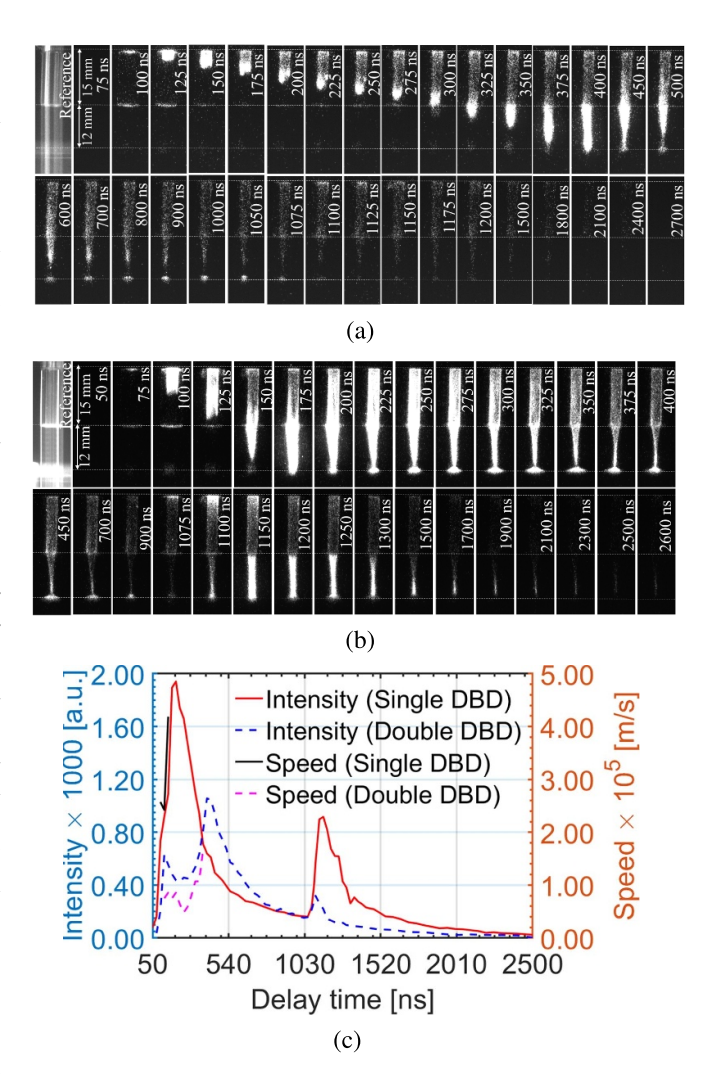
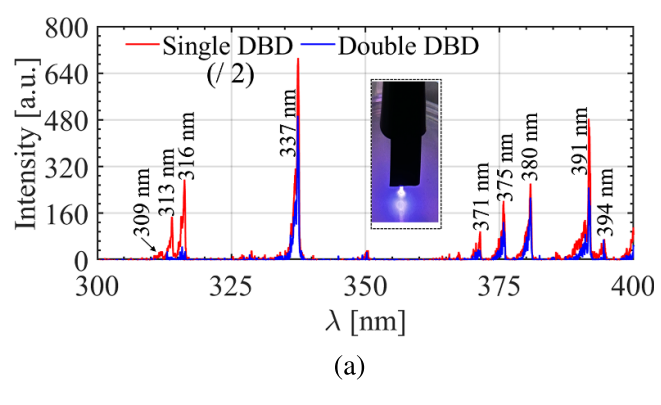


Figure 6. Temporal evolution of plasma bullets in a (a) double DBD and (b) single DBD plasma jet in contact with water surface. The first dotted line on each rows represent the bottom of the ground electrode, the second dotted line represents the nozzle of the quartz tube and the third dotted line represents the surface of water. Each image is obtained with single shot at a TTL gate width of 30 ns and exposure time of 1 μ s (Operating conditions: applied voltage—7 kV, frequency—6 kHz, pulse width—1 μ s, He flow rate—2 SLPM). A plot of pixel intensities and propagation speeds computed from corresponding images in (a), (b) are shown in (c).

electrode and becomes weaker after 1175 ns. Similarly, the mechanism of plasma bullet propagation in the single DBD plasma jet in contact with water surface is represented in figure 6(b). The first emission below the ground electrode is detected at a delay time of 75 ns. It then continues propagation along the quartz tube and towards the surface of water. By 150 ns, the plasma bullet already crosses the nozzle of the quartz tube and it splashes in water before 175 ns. Similar to double DBD configuration, the propagation speed is seen to increase when the plasma bullet approaches the surface of water. The propagation of the bullet before splashing into water was measured to be 4.20×10^5 m s⁻¹. As the bullet splashes in water (175 ns), the discharge region between the main ground electrode and the surface of water appears with



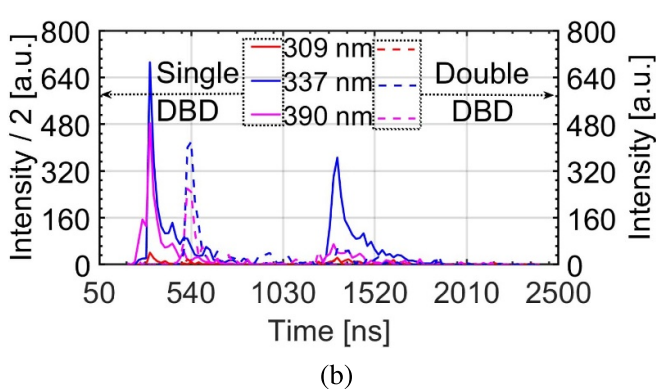


Figure 7. (a) Optical emission spectra of the discharge between 300 and 400 nm for the double and single DBD plasma jets in contact with water surface. The spectrums recorded at central wavelengths of 309 nm, 337 nm and 375 nm were combined in order to obtain the plot. The intensities for single DBD configuration have been reduced by half in order to show the emissions clearly in the same scale. Only the emission from the interface region was acquired and the upper area was blocked (see inset image for the single DBD configuration). (b) Time-resolved optical emission intensities for the two jet configurations at 309 nm, 337 nm and 390 nm. Operating conditions: applied voltage—7 kV, frequency—6 kHz, pulse width—1 µs, He flow rate—2 SLPM.

a bright emission. This brightness continues for the next 25 ns probably due to the ionization of water molecules and subsequent emission from excited species. After 200 ns, the discharge intensity decreases. At 1075–1100 ns, another emission is below the ground electrode and above the surface of water. The intensity of the secondary emission is much brighter than the double DBD configuration and this lasts until 2200 ns. The formation of secondary discharge is due to the accumulated charges that were formed on the inner surface of the quartz tube and inside the surface of water (figure 4). The higher emission intensity is thus attributed to the higher accumulation of charges. The secondary discharge emission above the surface of water for the double DBD configuration was weak. This is probably due to the lesser charges accumulated on the surface of water or the acquition settings used in the camera were not optimum to detect them.

3.4. Optical characteristics

3.4.1. Optical emission spectra. Figure 7(a) shows the OES of the discharge recorded in the range of 300–400 nm for the double and single DBD plasma jets. The optical fiber was

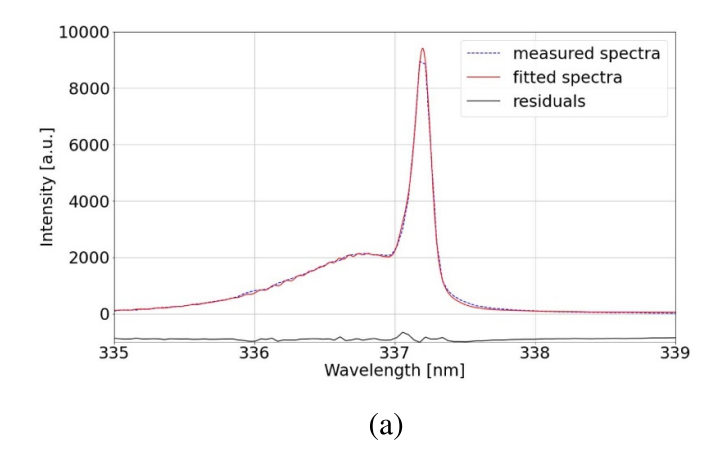
inclined at an angle of 45° and focused to the plasma-water interface (see inset image) to only obtain the spectra from the interface region. The region between 300 and 400 nm is mostly composed of the emissions from hydroxyl radical (${}^{\bullet}$ OH) at \approx 309 nm, several bands of nitrogen second positive system (N₂ SPS, 313 nm, 316 nm, 337 nm, 371 nm, 375 nm, 380 nm, 394 nm, etc), and nitrogen first negative system (N2 FNS, \approx 394 nm) [16, 30, 31]. Emissions from hydroxyl radicals appear due to the dissociation of water vapor molecules present in the feeding gas or in the ambient environment. The emissions from excited nitrogen is due to the dissociation of nitrogen molecules present in the ambient environment. In figure 7, it can also be observed that the optical emission intensities at all wavelengths for the single DBD configuration are higher than the double DBD configuration. These higher intensities could be the result of higher concentrations of short lived RONS formed during the discharge.

We also observed the temporal evolution of 309 nm OH, 337 nm N_2 and 391 nm N_2^+ at the plasma-water interface and these results are presented in figure 7(b). Similar to figure 6(b), two maxima are observed from each species. The first maxima corresponds to the emission from excited species formed during the rising part of the applied voltage. The second maxima is from the discharge caused by the accumulated charges. For all three wavelengths, the emission intensities from single DBD plasma jet are higher than the double DBD one. The peak emission intensities from 309 nm OH, 337 nm N₂ and 391 nm N_2^+ for the single and double DBD plasma jets appear at delay times of 320 ns and 520 ns respectively. The peak plasma bullet intensities for the single and double DBD jets in figure 6(b) also occur at an interval of 200 ns. This suggests that the delay in the occurrence of optical emission intensities for the double DBD configuration are caused by the slower motion of the plasma bullet.

In the next step, we utilized the intensity ratios from two optically closed lines corresponding to 391.4 nm N_2^+ FNS and 394.3 nm N_2 SPS ($R_{391/394}$) to get an estimate of the reduced electric field for the double and single DBD plasma jets [32]. This technique relies on the measurement of the ratio of intensities of two optical transitions with different thresholds/cross-sections and relates the ratio to the electric field knowing the dependence of rates of excitation by electron impact, radiative lifetime and the quenching rates. Assuming that excitation takes place by direct electron impact with the ground state of molecular nitrogen and the decay of the emitting states takes place by natural radioactive decay & collisional quenching by N_2/O_2 molecules, the calculation of reduced electric field can be made as [32, 33]:

$$R_{391/394} \left(\frac{E}{N}\right) = 46 \exp\left[-89 \left(\frac{E}{N}\right)^{-0.5}\right]$$
 (2)

where $(\frac{E}{N})$ is the reduced electric field strength. The values of electric field derived from equation (2) are found to be 806.27 \pm 128.06 Td 1269.20 \pm 133.20 Td respectively for the double and single DBD plasma jets respectively. The intensity ratios of 391 nm N_2^+ FNS to 337 nm N_2 SPS (figure 7) are also higher for single DBD configuration supporting our observations for



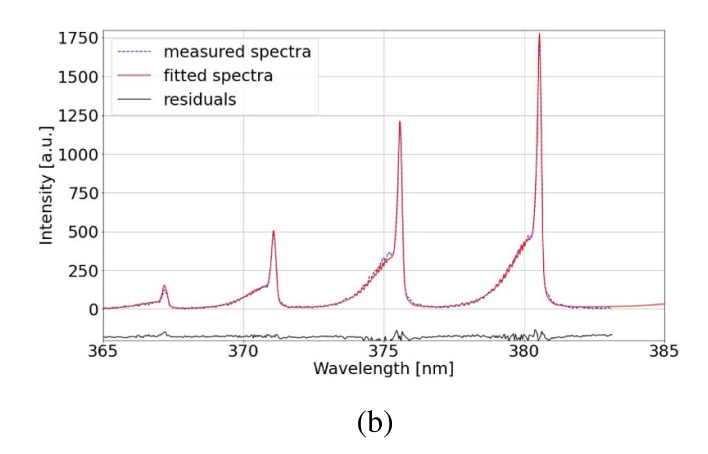


Figure 8. Sample fits of (a) 337 nm N_2 SPS; (b) 365–380 nm N_2 SPS bands obtained with MASSIVEOES for the determination of rotational and vibrational temperatures respectively. The sample spectra are obtained with the single DBD plasma jet in contact with water surface.

higher electric field. Additionally, the electric field strength in APPJs is also determined from the intensity ratios of 667.8 nm He to 728.1 nm He emissions ($R_{667.8/728.1}$) [34]. The average ratios of $R_{667.8/728.1}$ for the single and double DBD configurations were measured to be 4.26 and 2.94 respectively. These results also provide additional support for higher electric field in single DBD plasma jet. The higher electric field could be related to our observations in figures 5–7. The shielding of the HV electrode in the double DBD configuration thus reduces the plasma potential and the electric field resulting in the slower propagation of plasma bullets & lower emission intensities from reactive species.

The OES recorded for the single/double DBD plasma jets were further utilized to estimate the rotational/vibrational temperature, electron density and electron temperature. These will be discussed in the next sections.

3.4.2. Rotational/Vibrational temperature. Because of the high collision frequency at atmospheric pressure, the translational temperature of the plasma is close to rotational temperature and can be approximated from the N_2 SPS emission [35]. The experimental spectra obtained from N_2

SPS were fitted by using a simulated spectra generated by MASSIVEOES developed by Vorac et al [36-38] and the results from best fit were used to estimate the rotational/vibrational temperature. A sample of the fitted spectrum of the N₂ SPS for the 337 nm band and the 365–380 nm bands for the single DBD configuration are shown in figures 8(a) and (b) respectively. The fitting from 337 nm N2 SPS band was used for the estimation of rotational temperature while the fitting from 365 to 380 nm N₂ SPS bands were used for the estimation of vibrational temperature. The rotational temperatures derived from the fitted spectra were obtained to be 305.57 \pm 9.29 K and 329.54 \pm 6.56 K for the double and single DBD plasma jets respectively. Similarly, the vibrational temperatures for the double and single DBD configurations were measured to be 3437.62 \pm 40.67 K and 4150.43 \pm 23.54 K respectively. A higher temperature for the single DBD configuration is attributed to be the result of higher discharge current (figure 3).

3.4.3. Electron density. Electron density (n_e) is a key parameter in APPJs as it strongly influences the discharge properties and formation of reactive oxygen and nitrogen species. A commonly used method for the determination of n_e is the atomic line stark broadening. This method is popular as it gives a straightforward relation between the line width caused by $n_{\rm e}$ and stark broadening. The atomic emission from hydrogen alpha (H_{α}) line at 656 nm was utilized to estimate the values of electron density for the two configurations of the plasma jets. At atmospheric pressure, its broadening is influenced by several effects which mainly include, Doppler broadening (caused by thermal motions of excited hydrogen atoms), Van der Waal's broadening (caused by the collision of excited hydrogen atoms with helium atoms), and instrumental broadening (the characteristic instrumental function of the optical system). Some other broadening mechanisms such as natural broadening (which arise due to the finite lifetime of the excited levels) and resonant broadening (occurring for transitions involving a level) due to their very small value are usually neglected. The profiles coming from these mechanisms can be well approximated to Gaussian (effect of Doppler and instrumental broadening) or Lorentzian (effect of Van der Waal's and stark broadening), and the combination of them (convolution) known as Voigt profile. The Gaussian profile was determined by both the Doppler and instrumental broadening, in which the full-width at half maximum (FWHM) of the Gaussian is given by [39]:

$$\Delta \lambda_{\rm G} = (\Delta \lambda_{\rm D}^2 + \Delta \lambda_{\rm I}^2)^2 \tag{3}$$

where $\Delta\lambda_D$ and $\Delta\lambda_I$ are the FWHM of the Doppler broadening and instrumental broadening respectively.

Doppler broadening $(\Delta \lambda_D)$ mainly depends upon the gas temperature (T_g) of the emitter and it is calculated by using the expression of its FWHM as [40]:

$$\Delta \lambda_{\rm D} = 7.16 \times 10^{-7} \lambda \left(\frac{T_{\rm g}}{M} \right) \tag{4}$$

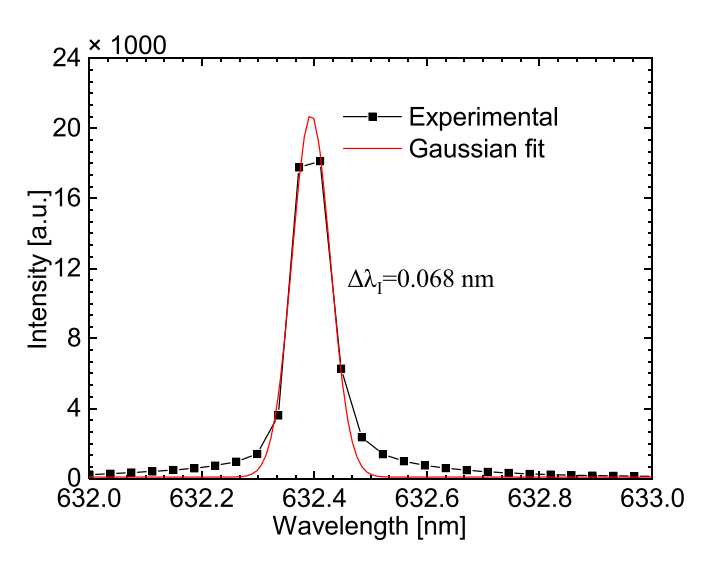


Figure 9. Determination of the instrumental broadening through Gaussian fit of the experimental spectrum. A monochromatic light emitted by He–Ne laser source was used for estimating the broadening.

where λ is the emission wavelength, T_g is the gas temperature of the plasma in kelvin and M is the atomic weight of hydrogen atoms in g mol⁻¹.

The determination of Van der Waals broadening $(\Delta \lambda_V)$ is done by the expression of its FWHM as [40]:

$$\Delta \lambda_V = K_{\rm i} \left(\frac{T_{\rm g}}{\mu}\right)^{0.3} N \tag{5}$$

where μ is the reduced mass of H–He pairs and N is the neutral density which can be obtained from the gas temperature T_g via the ideal gas law. K_i is a constant depending on the spectral line and emitter polarizability. For plasmas operating in air with helium as the working gas, equation (5) is reduced to the following form [39, 41]:

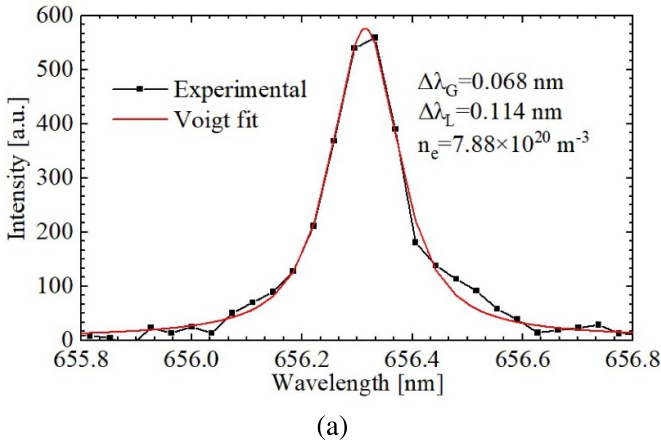
$$\Delta \lambda_V = \frac{2.42}{T_g^{0.7}}.\tag{6}$$

The instrumental broadening is determined by measuring the FWHM of the He–Ne laser source (Model no: 05-LLP-805, Melles Griot) at a wavelength of 632.4 nm. The slit width in the spectrometer was 25 μ m and a grating with 1200 lines mm⁻¹ was used. A fit of the experimental spectrum is shown in figure 9. The value of instrumental broadening is obtained as:

$$\Delta \lambda_{\rm I} = 0.068 \text{ nm}. \tag{7}$$

The value of stark broadening $\Delta \lambda_S$ is obtained from the FWHM of Lorentzian broadening $\Delta \lambda_L$ and Van der Waals broadening by using following expression [40]:

$$\Delta \lambda_{\rm S} = \Delta \lambda_{\rm L} - \Delta \lambda_{\rm V}. \tag{8}$$



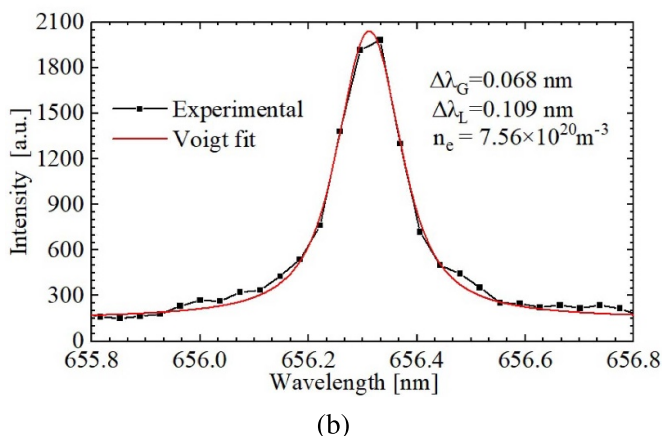


Figure 10. Voigt fit of the experimental H_{α} emission at 656 nm for the (a) double DBD and (b) single DBD plasma jet. Both spectra were recorded at the plasma water interface. Operating conditions: applied voltage—7 kV, frequency—6 kHz, pulse width—1 μ s, He flow rate—2 SLPM.

In equation (8), $\Delta \lambda_L$ is obtained from the Voigt fit of the experimental spectrum and $\Delta \lambda_V$ is obtained from equation (6). The Voigt fits of the experimental spectrum for the double and single DBD plasma jets are shown in figures 10(a) and (b) respectively.

Finally, the value of electron density is obtained using the following expression [39]:

$$\Delta \lambda_{\rm S} = 1.78 \times \left(\frac{n_{\rm e}}{10^{23} {\rm m}^{-3}}\right). \tag{9}$$

The values of electron densities calculated using equation (9) for the double and single DBD configurations are found to be $7.49 \pm 0.86 \times 10^{20}$ m⁻³ and $7.30 \pm 0.23 \times 10^{20}$ m⁻³ respectively, (figure 10).

3.4.4. Excitation temperature. The generation of active species through collisions and subsequent production of reactive species are essentially controlled by electron temperature and electron density. For a plasma in local thermodynamic equilibrium (LTE), a Boltzmann plot of the excited emission

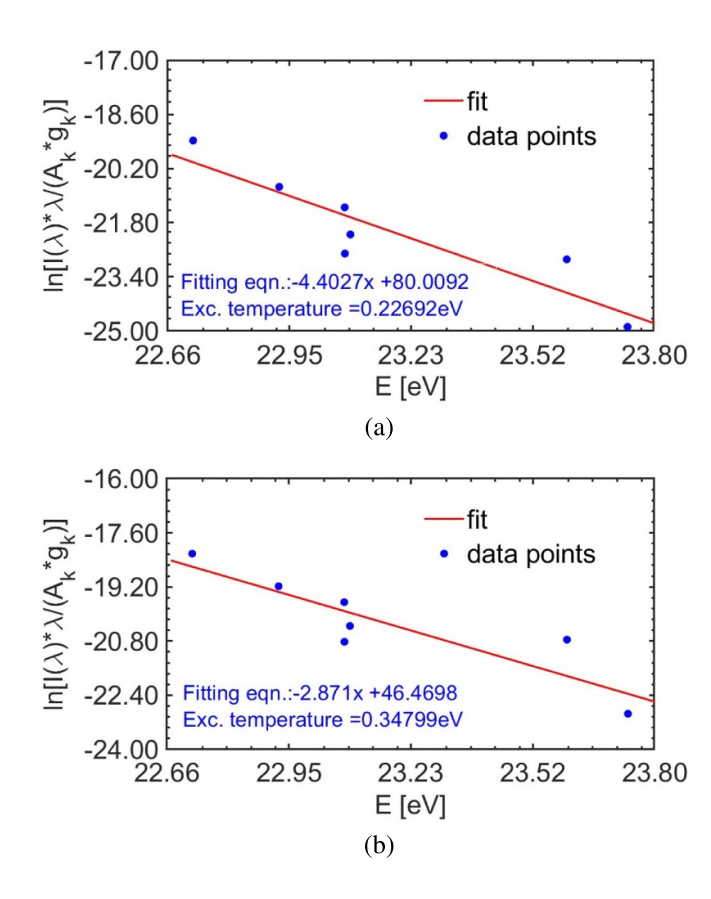


Figure 11. Excitation (Exc.) temperature measured using excited helium emission lines for the (a) double DBD and (b) single DBD plasma jet at plasma-water interface.

lines derived from the OES measurement could be used for the determination of electron temperature. But, for a plasma in non-LTE this method could give an approximation of excitation temperature ($T_{\rm exc}$) [42, 43]. Intensities from several excited helium lines (471.31 nm, 492.19 nm, 501.57 nm, 587.56 nm, 667.80 nm, 706.52 nm and 728.13 nm) were included in the model assuming a Boltzmann distribution of the population of the atomic level as [42]:

$$\ln\left(\frac{I\lambda}{g_k A_k}\right) = -\frac{E}{k_{\rm B}T} + C \tag{10}$$

where λ is the wavelength, I is the measured intensity, A_k is the transition probability, g_k is the statistical weight of the upper level, E is the energy level of the upper level, K_B Boltzmann's constant and T is the temperature in Kelvin. The slope of the straight line $(\frac{1}{k_BT})$ obtained from equation (10) gives the value of excitation temperature. Typical Boltzmann plots obtained with excited helium emission lines are shown in figure 11. Some of the points in the plot appear away from the line of best fit as the effect of collisional quenching in the calculation have not been considered. The slopes of the straight lines yield the value of excitation temperature to be 0.34 ± 0.03 eV (figure 11(a)) and 0.24 ± 0.02 eV (figure 11(b)) respectively for the double and single DBD plasma jets.

3.5. Measurement of H₂O₂ & NO₂ concentrations in PAW

H₂O₂ is major long-lived reactive species formed by APPJs and it is known to be a broad spectrum antimicrobial agent. It arises from reactions with radicals formed within the core of the plasma discharge from recombination reactions between OH radicals and in the plasma effluent as oxygen from air mixes and reacts with atomic hydrogen and hydroperoxyl radical [20]. The calibration curve used for measuring H₂O₂ concentration in PAW is presented in figure 12(a) and the results showing the effect of plasma exposure time for the double and single DBD configurations of the plasma jets are shown in figure 12(b). For both configurations, the concentration of H₂O₂ increased with plasma exposure time. The H₂O₂ concentrations for the 3 min and 5 min plasma exposure time increased by $\approx 126\%$ and $\approx 179\%$ respectively as compared to 1 min plasma exposure time for the double DBD plasma jet. The corresponding increments for the single DBD configuration were \approx 52% and \approx 82% respectively. For all plasma exposure time, the concentration of H₂O₂ for the single DBD plasma jet was more than two times higher than the single DBD one.

Similarly, the effect of increasing He flow rate from 2 to 4 SLPM on the production of H_2O_2 is represented in figure 12(c). For single DBD configuration, an increase in gas flow rate also leads to the significant increase in H_2O_2 concentration from \approx 625 μ M to \approx 875 μ M. On the other hand, the increase in gas flow does not significantly increase the production of H_2O_2 for the double DBD configuration and it remains constant at \approx 300 μ M.

We also investigated the quantitative formation of NO_2^- in plasma activated water for the double and single DBD configurations of the plasma jets. These results are shown in figure 12(d). The colour changes for the single DBD configuration at all plasma exposure times $(1, 3, 5 \, \text{min})$ are stronger than the double DBD configuration. These results indicate that the formation of nitrates and nitrates could also be higher for single DBD configuration.

The formation of H_2O_2 in APPJs is mainly attributed to the presence of water vapor molecules which may be present in the feeding gas or adsorbed inside the gas tubing. The working gas used in this study (99.999% He) contained ≈ 1 ppm of moisture. The experiment was conducted at a humidity of $\approx 36\%$. Water vapor molecules are firstly dissociated into highly reactive $^{\bullet}OH$ radicals which subsequently combine to form H_2O_2 mainly through the following mechanisms [17, 44–49]:

- (a) Collisions with electrons: $e^- + H_2O \rightarrow {}^{\bullet}H + {}^{\bullet}OH + e^-$
- (b) Collisions with metastable atoms/radicals: $e^- + O_2 \rightarrow O(^3P) + O(^1D) + e^-, O(^1D) + H_2O \rightarrow 2^{\bullet}OH; e^- + N_2 \rightarrow N_2(A^3\sum_u^+) + e^-, N_2(A^3\sum_u^+) + H_2O \rightarrow ^{\bullet}OH + N_2 + ^{\bullet}H$
- (c) Collision with helium metastables: $e^- + He \rightarrow He_m + e^-$; $He_m + H_2O \rightarrow He + H_2O^+ + e^-$; $e^- + H_2O^+ \rightarrow {}^{\bullet}OH + {}^{\bullet}H$
- (d) Plasma initiated ultraviolet photolysis: UV + $H_2O \rightarrow H_2O^*$; UV + $H_2O^* \rightarrow H^+ + OH^-$; $OH^- \rightarrow OH^+ e^-$

The OH radicals formed through mechanisms (a)–(d) recombine to form H_2O_2 as: ${}^{\bullet}OH + {}^{\bullet}OH \rightarrow H_2O_2$.

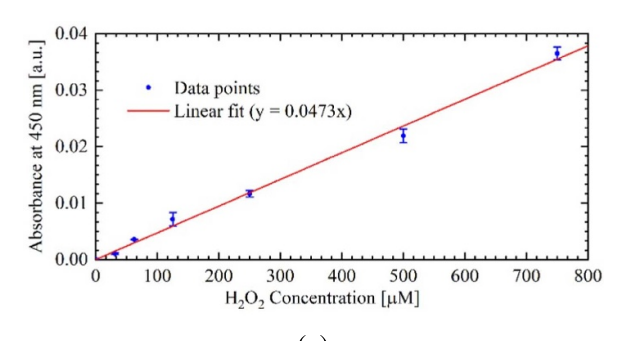
On the other hand, the formation of NO_2^- in APPJs takes place through the recombination of atomic oxygen (O) and atomic nitrogen (N) as [44, 50]:

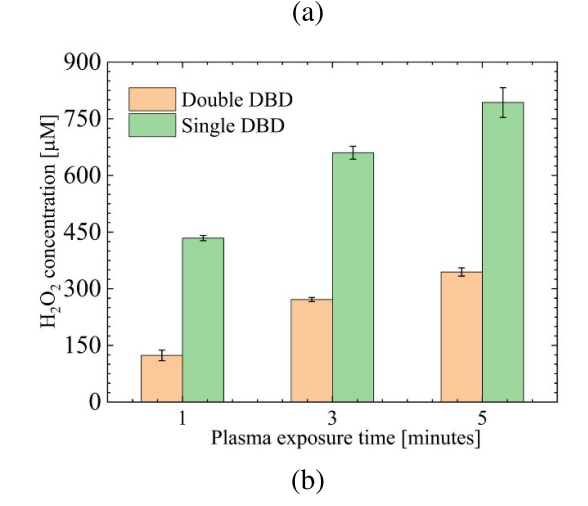
- (e) N+O₂ → NO + O; N + •OH → NO + •H; N+O → NO Nitric oxide (NO) thus formed in (e) recombines with O₂ and H₂O to form NO₂⁻ [20]:
- (f) $4NO + 2O_2 + 2H_2O \rightarrow NO_2^- + 4H^+$

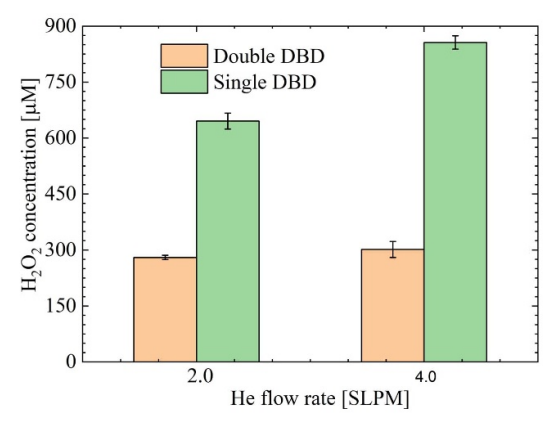
The production of RONS through collisions of electrons or ions with neutral atoms or metastables is mainly controlled by electron density and electron temperature. A higher electron density increases the number of collisions that take place with the neutral molecules. And the RONS formation mechanisms mentioned in (a)–(f) are enhanced at higher electron energies. The calculation of electron density using the method of Stark broadening in figures 10(a) and (b) suggests that they are close to each other. However, the value of excitation temperature, an indication of the electron temperature (figures 11(a) and (b)) obtained for the single DBD configuration is $\approx 0.10 \text{ eV}$ higher than the double DBD configuration. Also, the results in figure 6 show that the plasma bullets in single DBD configuration travel significantly faster and result in greater accumulation of charges inside the water (figure 4). From these results we conclude that high energy electrons travelling with higher velocity result in the higher production of H₂O₂ & NO₂ with the single DBD configuration of the plasma jet. Also, continuous exposure of water to the plasma increases the accumulation of plasma derived species (mainly H₂O₂, NO₂, NO, etc) which could be formed through the dissociation of ambient species in the plasma liquid interface) resulting in the higher concentration with time (figures 12(b) and (d)). Previous investigations on the effect of gas flow rate suggest that H₂O₂ concentration increase with increasing gas flow rate [20]. A higher gas flow rate increases the speed of delivery of hydroxyl radicals to the target solution by minimizing the quenching reactions of hydroxyl radicals with ambient air molecules. This was not significant for the double DBD configuration of the plasma jet in the present study (figure 12(c)) due to the lower energy of electrons.

3.6. Application to bacterial killing

The final set of experiments involved investigating the bactericidal efficacy of the double and single DBD plasma jets. Non-pathogenic *E. coli* were grown and distributed on agar surface of petri-dishes as described in Experimental Methodology. The bacterial cells were then treated by both plasma jets at a target-nozzle distance of 12 mm by varying plasma exposures time (1, 3 and 5 min), He flow rate (2, 4 SLPM) and bacterial cell density (10² CFU cm⁻², 10⁴ CFU cm⁻² and 10⁶ CFU cm⁻²). At identical values of operating conditions, the diameter of the plasma in contact with the agar was similar to water figure 2. However, the brightness was observed







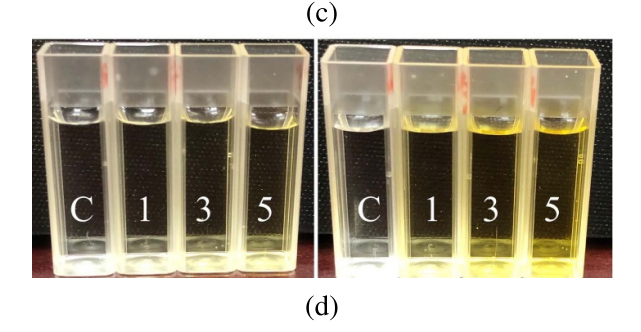


Figure 12. Measurement of H_2O_2 & NO_2^- in PAW (a) calibration curve constructed with known concentrations of H_2O_2 ; (b) effect of plasma exposure time; (c) effect of increasing the gas flow rate from 2 to 4 SLPM for both double and single DBD plasma jets (plasma exposure time = 3 min); and (d) Visualisation of NO_2^- formation with double (left) and single (right) DBD plasma jets (where C =control & 1,3,5 = plasma exposure times).

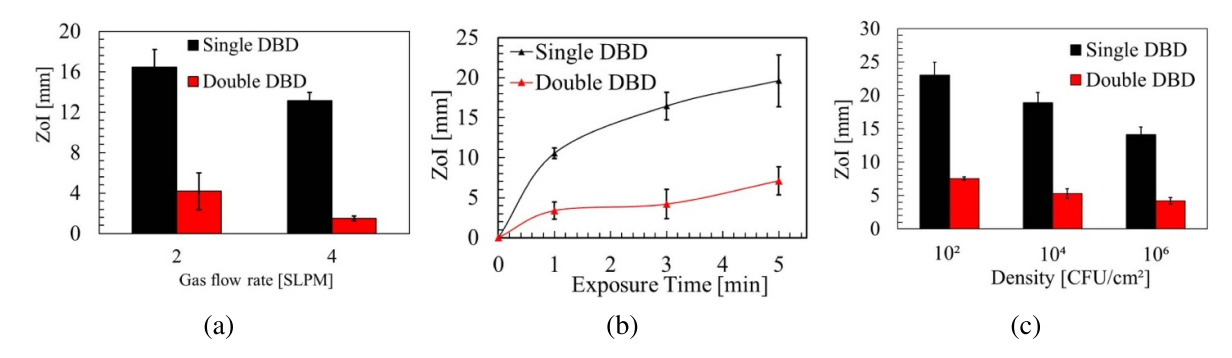


Figure 13. Evaluating the bacterial inactivation efficacy of double and single DBD plasma jets—(a) effect of plasma exposure time (1, 3, and 5 min); (b) effect of 2,4 SLPM He flow (plasma exposure time = 3 min); and (c) effect of varying bacterial cell densities (exposure time = 3 min, He flow rate = 2 SLPM, applied voltage = 7 kV pulsed DC).

to be higher with the single DBD configuration. The bactericidal efficacy was analyzed through the measurement of zone of inhibition (ZoI).

Increasing plasma exposure times from 1 to 5 min led to almost doubling of the average ZoI (i.e. from ≈ 10.5 mm to ≈ 20 mm for the single DBD configuration, figure 13(a)). Efficiency of the shielded configuration is lower by at least three times for all plasma exposure times. These observations correlate well with the observed concentrations of H_2O_2 shown in figure 12(b). Increasing the He flow rate from 2 to 4 SLPM resulted in a slight decrease of bactericidal efficiency but for both gas flow rates, single DBD configuration is still more efficient (figure 13(b)). We also tested whether the single DBD configuration performance depends on the bacterial cell density. Comparing three cell densities at otherwise fixed plasma operating conditions showed that efficiency of plasma killing decreases at higher densities of cells as expected, but the single DBD configuration remains more efficient (figure 13(c)).

Taken together, these results show that single DBD configuration of the plasma jet achieves better decontamination results in a fraction of time required for the double DBD configuration. This is attributed to the higher production of H_2O_2 alongwith other RONS and higher temperature of the jet.

4. Conclusions

In conclusion, the characteristics of two APPJs operated with single and double dielectric materials in contact with water surface were investigated. Results from electrical measurements showed that the accumulation of charges onto the surface of water could be significantly higher with the single DBD configuration of the plasma jet. The higher accumulated charges result from the higher plasma potential which in the double DBD configuration is reduced by the quartz tube shielding the high voltage electrode. The time-resolved images obtained with the ICCD camera showed that plasma bullets in a single DBD plasma jet travel by an order of magnitude faster than those in the double DBD plasma jet. Because of this the emissions from the excited species at the water-interface occurred earlier with the single DBD plasma jet. Results

from optical emission spectroscopy showed stronger emissions from short lived reactive species, mainly hydroxyl radicals and excited nitrogen species at the outlet of both plasma jets, and the intensities were observed to be higher for the single DBD configuration. Analysis of the OES for rotational temperature showed that the single DBD plasma jet operates at significantly higher temperature close to the water interface making it unsafe for direct biological treatments. Also, the electric field measured from the optical emission spectroscopy was found to be higher for the single DBD configuration. The higher electric field resulted from the higher electron energy which was confirmed with the measurement of excitation temperature of the excited helium emissions although the electron densities for two configurations were similar to each other. These characteristics of single DBD configuration resulted in the formation of more than double hydrogen peroxide concentration inside plasma activated water and the results correlated well with the bactericidal effects against E. coli through direct plasma treatment. Our results show that the higher electric field caused through higher accumulation of wall charges influence the physical and chemical characteristics of the plasma jet that may have significant impact on several biomedical applications. The present study suggests these impacts could be stronger with an single DBD plasma jet.

Data availability statement

All data that support the findings of this study are included within the article.

Acknowledgments

This work was supported by the NSF EPSCOR RII-Track-1 Cooperative Agreement OIA-1655280 and DOE DE-SC0021391. Any opinions, findings, and conclusions or recommendations expressed in this material are those of the author(s) and do not necessarily reflect the views of the National Science Foundation.

ORCID iDs

Bhagirath Ghimire https://orcid.org/0000-0002-5243-8528

Elanie F Briggs https://orcid.org/0000-0003-3856-4875 Tatyana A Sysoeva https://orcid.org/0000-0003-1522-0041

John A Mayo https://orcid.org/0000-0002-9772-5504 Kunning G Xu https://orcid.org/0000-0002-1249-0380

References

- [1] Isbary G et al 2013 Clin. Plasma Med. 1 25
- [2] Percival S L, Vuotto C, Donneli G and Lipsky B A 2015 Adv. Wound Care 4 389
- [3] Isbary G et al 2010 Br. J. Dermatol. 163 78
- [4] Nasruddin, Nakajima Y, Mukai K, Rahayu H S E, Nur M, Ishijima T, Enomoto H, Uesugi Y, Sugama J and Nakatani T 2014 Focus Issue-Plasma Dentistry 2 2212
- [5] Isbary G et al 2012 Br. J. Dermatol. 167 404
- [6] Stratman B et al 2012 JAMA Network Open 3 1
- [7] Lu X, Naidis G V, Laroussi M, Reuter S, Graves D B and Ostrikov K 2016 *Phys. Rep.* **630** 1
- [8] Laroussi M et al 2022 IEEE Trans. Radiat. Plasma Med. Devices 6 127
- [9] Labay C, Roldan M, Tampieri F, Stancampiano A, Bocanegra P E, Ginebra M-P and Canal C 2020 ACS Appl. Mater. Interfaces 12 47256–69
- [10] Prochnow A M, Clauson M, Hong J and Murphy A B 2016 Sci. Rep. 6 1
- [11] Lu X, Laroussi M and Puech V 2012 Plasma Sources Sci. Technol. 21 034005
- [12] Winter J, Brandenburg R and Weltmann K-D 2015 *Plasma Sources Sci. Technol.* **24** 064001
- [13] Brandenburg R 2018 Plasma Sources Sci. Technol. 27 079501
- [14] Lu X, Jiang Z, Xiong Q, Tang Z and Pan Y 2008 Appl. Phys. Lett. 92 151504
- [15] Lu X, Jiang Z, Xiong Q, Tang Z, Hu X and Pan Y 2008 Appl. Phys. Lett. 92 081502
- [16] Ghimire B, Lamichhane P, Lim J S, Min B, Paneru R, Weltmann K-D and Choi E H 2018 Appl. Phys. Lett. 113 194101
- [17] Gott R P and Xu K G 2019 IEEE Trans. Plasma Sci. 47 4988
- [18] Gott R P and Xu K G 2020 J. Phys. D: Appl. Phys. 53 315201
- [19] Gott R P, Thompson M E, Staton B C, Williams B M and Xu K G 2021 *IEEE Trans. Plasma Sci.* **49** 2113
- [20] Ghimire B et al 2021 Plasma Sources Sci. Technol. 30 035009
- [21] Girard F et al 2018 RSC Adv. 20 9198
- [22] Szili E J, Ghimire B, Patenall B L, Rohaim M, Mistry D, Fellows A, Munir M, Jenkins A T A and Short R D 2019 Appl. Phys. Lett. 119 054104
- [23] Jogi I, Talviste R, Raud S, Raud J, Plank T, Moravsky L, Klas M and Matejcik S 2020 Appl. Sci. 60 201900127

- [24] Yambe K, Taka S and Ogura K 2014 *IEEJ Trans. Electr. Electron. Eng.* **9** 13
- [25] Klarenaar B L M, Guaitella O, Engeln R and Sobota A 2018 Plasma Sources Sci. Technol. 27 085004
- [26] Sretenovic G B, Krstic I B, Kovacevic V V, Obradovic B M and Kuraica M M 2010 J. Phys. D: Appl. Phys. 47 355201
- [27] Ji L, Xia Y, Bi Z, Niu J and Liu D 2015 *AIP Adv.* **5** 087181
- [28] Karakas E and Laroussi M 2010 J. Appl. Phys. 108 063305
- [29] Karakas E, Akman M and Laroussi M 2012 Plasma Sources Sci. Technol. 21 034016
- [30] Sarani A, Nikiforov A Y and Leys C 2010 Phys. Plasmas 17 063504
- [31] Gazeli K, Noel C, Clement F, Dauge C, Svarnas P and Belmonte T 2013 Plasma Sources Sci. Technol. 22 025020
- [32] Paris P, Aints M, Valk F, Plank T, Haljaste A, Kozlov K V and Wagner H -E 2005 J. Phys. D: Appl. Phys. 38 3894
- [33] Goldberg GB M, Hoder T and Brandenburg R 2022 J. Phys. D: Appl. Phys. 31 073001
- [34] Ivkovic S S, Sretenović G B, Obradović B M, Cvetanović N and Kuraica M M 2014 J. Phys. D: Appl. Phys. 47 055204
- [35] Jin D J, Uhm H S and Cho G S 2013 *Phys. Plasmas* **20** 083513
- [36] Vorac J, Kusyn L and Synek P 2019 Rev. Sci. Instrum. 19 123102
- [37] Vorac J, Synek P, Prochazka V and Hoder T 2017 J. Phys. D: Appl. Phys. 50 294002
- [38] Vorac J Synek P, Potocnakova L, Hnilica J and Kudrle V 2017 Plasma Sources Sci. Technol. 30 025010
- [39] Li S, Liu Y, Yuan H, Liang J, Zhang M, Li Y and Yang D 2022 Appl. Sci. 12 8895
- [40] Qian M, Ren C, Wang D, Zhang J and Wei G 2010 J. Appl. Phys. 107 063303
- [41] Hofmann S, Gessel A F H V, Verreycken T and Bruggeman P 2011 Plasma Sources Sci. Technol. 20 065010
- [42] Gulec A, Bozduman F and Hala A M 2015 IEEE Trans. Plasma Sci. 43 786
- [43] Yambe K and Satou S 2016 Phys. Plasmas 23 023509
- [44] Kaushik N K et al 2019 Biol. Chem. 400 39
- [45] Pei X, Lu Y, Wu S, Xiong Q and Lu X 2013 *Plasma Sources Sci. Technol.* 22 025023
- [46] Ghimire B, Szili E J, Lamichhane P, Short R D, Lim J S, Attri P, Masur K, Weltmann K-D, Hong S-H, Choi E H 2019 Appl. Phys. Lett. 114 093701
- [47] Uhm H S 2015 Phys. Plasmas 22 123506
- [48] Bolouki N, Kuan W-H, Huang Y-Y and Hsieh J-H 2021 *Appl. Sci.* **11** 6158
- [49] Ghimire B, Szili E J and Short R D 2022 Appl. Phys. Lett. 121 084102
- [50] Uchida G, Nakajima A, Ito T, Takenaka K, Kawasaki T, Koga K, Shiratani M and Setsuhara Y 2016 J. Appl. Phys. 120 203302